Remote generation of modulators for super-resolution imaging

Jian-yu Lu ⬤

🔴 Check for updates

🌐 View Online   ↗ Export Citation

Articles You May Be Interested In

Focused beams for high-resolution imaging and other applications

Proc. Mtgs. Acoust. (March 2022)

A beamforming algorithm with composite multi-conditional cross correlation and range standard deviation factor for high quality ultrasound imaging

J. Acoust. Soc. Am. (April 2025)

A modified sidelobe blanking beamforming method for ultrasound plane wave imaging

J. Acoust. Soc. Am. (August 2024)

Remote generation of modulators for super-resolution imaging

Jian-yu Lu
Department of Bioengineering, The University of Toledo, Toledo, OH, 43606; jian-yu.lu@ieee.org

In 1873, Ernst Abbe found a diffraction-limited resolution of about 200 nm for conventional optical microscopes. Many methods to overcome the limit (super-resolution) have been developed. Recently, a general super-resolution imaging method was developed based on the theory of linear-shift-invariant (LSI) system and modulation of the system point-spread-function (PSF) (Lu, IEEE TUFFC, Jan. 2024), which has broad applications in various disciplines of science, engineering, and medicine. In this paper, focused shear waves generated remotely by radiation force were studied comprehensively via theoretical analyses and computer simulations to modulate the imaging waves or the PSF of imaging systems such as those of B-mode and photoacoustics for super-resolution imaging. A method to reduce sidelobes and thus increase the contrast of super-resolution images was developed. Atomic imaging with small physical particles such as optically opaque ions was suggested. It is found that focused shear waves can be produced with an annular, 2D, or 1D array transducer; with a conventional focused beam; or with local vibration sources. Also, they can resonate to increase signal-to-noise ratio (SNR). This study paves a way for super-resolution imaging of mechanical properties (related to shear-wave amplitude, attenuation, speed, spectrum, and nonlinearity) of biological soft tissues deep in the body.

28 November 2025 09:00:56

1. INTRODUCTION

In 1873, Ernst Abbe found that the conventional optical microscopes have a diffraction limited resolution of about 200 nm [1]. Methods to overcome the limit (super-resolution) have been developed [2]-[12], including the 1994 stimulated emission depletion (STED) [13] and 2006 photoactivated localization microscopy (PALM) [14] that won the 2014 Nobel Prize in Chemistry. However, these methods image the distributions of fluorescent molecules [13]-[14], microbubbles [8]-[10], or were developed for specific applications [2]-[7], [11]-[12]. Recently, a general super-resolution imaging method was developed by the author based on the theory of linear shift-invariant (LSI) system and modulation of the system point spread function (PSF) [15]. Since many practical imaging systems are LSI or can be approximated as an LSI system, the method can have broad applications in various disciplines of science, engineering, and medicine [15]-[18].

Based on the method in Ref. [15], in this paper, focused shear waves were studied in details as modulators both theoretically and with computer simulations for low-sidelobe and high-contrast super-resolution imaging of mechanical properties (related to shear-wave amplitude, attenuation, speed, spectrum, and nonlinearity) of biological soft tissues deep in the body if the half wavelength of the shear waves is smaller than the size of the PSF of the imaging system. These studies show that the focused shear waves can be produced remotely by focused Bessel (forming a cylindrical ring of radiation force [19]-[21]) or cosine [22] (forming plates of radiation force) beams with an annular (can be steered mechanically [20]), two-dimensional (2D), or one-dimensional (1D) array transducer or produced locally by other vibration sources to modulate the imaging waves or the PSF of imaging systems such as pulse-echo B-mode, photoacoustic [23], and non-destructive evaluation (NDE) [24] imaging.

Note that since the conventional focused plane wave is a special case of the focused Bessel or cosine beam with their scaling parameters set to zero [20], it also can be used to produce focused shear waves for super-resolution imaging, which minimizes the effects of shear wave attenuation [25]. In addition, the focused shear waves can produce high resonance peaks under certain boundary conditions, which increase shear-wave amplitude for imaging of nonlinear properties of objects and improving the signal-to-noise ratio (SNR) of the imaging systems. Such boundary conditions can be realized with phased-locked radiation force [26], fixed amplitude or stress at the boundaries, or other mechanisms [27]. Finally, the sensitivity and dynamic range of the imaging systems, and thus the resolution of super-resolution images, can be greatly increased if the imaging waves modulated at different times can interfere coherently before being detected. In addition to the focused shear waves, the modulators can be small physical particles such as nanoparticles (or optically opaque ions for optical atomic imaging) [15].

2. THEORETICAL DEVELOPMENT

A. NAVIER-CAUCHY EQUATION FOR ISOTROPIC AND LINEAR ELASTICITY

To use shear wave as a remote modulator for super-resolution imaging, it is necessary to understand its behaviors. The Newton's second law for a small volume of material (equation of motion) is given by [27]:

$$\rho(\vec{r};t)\frac{\partial^2 \vec{s}\,'(\vec{r};t)}{\partial t^2} = \nabla \cdot \boldsymbol{\sigma}(\vec{r};t) + \vec{q}\,'(\vec{r};t)\,, \tag{1}$$

where $\rho(\vec{r};t)$ is density, $\vec{s}\,'(\vec{r};t)$ is displacement vector, "$\nabla\cdot$" is the divergence in terms of $\vec{r}$, $\boldsymbol{\sigma}(\vec{r};t)$ is a stress tensor, $\vec{q}\,'(\vec{r};t)$ is a force per unit volume or volumetric force (such as radiation force of acoustic or optic waves), $\vec{r} = (x_0, y_0, z)$ is a spatial position in rectangular coordinates (see coordinates in Figs. 1(a) and 1(b)), and t is the time. According to Hooke's Law (stress-strain relationship) in isotropic linear elastic media, we have [27]:

$$\boldsymbol{\sigma}(\vec{r};t) = \gamma[\nabla \cdot \vec{s}\,'(\vec{r};t)]\mathbf{I} + 2\mu\boldsymbol{\varepsilon}(\vec{r};t)\,, \tag{2}$$

where γ is the first Lame constant, μ is the second Lame constant or shear module, $\mathbf{I}$ is a unit (identity) tensor, and $\boldsymbol{\varepsilon}(\vec{r};t)$ is a strain tensor (a relative dimension change):

$$\boldsymbol{\varepsilon}(\vec{r};t) = \{\nabla \vec{s}\,'(\vec{r};t) + [\nabla \vec{s}\,'(\vec{r};t)]^T\}/2\,, \tag{3}$$

where ∇ is a gradient in terms of $\vec{r}$, and T means transpose. Inserting Eqs. (2) and Eq. (3) into Eq. (1), we obtain the Navier-Cauchy equation for isotropic and linear elasticity if the media is approximately incompressible:

$$\rho(\vec{r};t)\frac{\partial^2 \vec{s}\,'(\vec{r};t)}{\partial t^2} = \nabla \cdot \{\gamma[\nabla \cdot \vec{s}\,'(\vec{r};t)]\mathbf{I} + 2\mu\varepsilon(\vec{r};t)\} + \vec{q}\,'(\vec{r};t) = \gamma\nabla[\nabla \cdot \vec{s}\,'(\vec{r};t)] + \mu\nabla^2 \vec{s}\,'(\vec{r};t) + \mu\nabla[\nabla \cdot \vec{s}\,'(\vec{r};t)] + \vec{q}\,'(\vec{r};t)$$

$$= \mu\nabla^2 \vec{s}\,'(\vec{r};t) + (\gamma + \mu)\nabla[\nabla \cdot \vec{s}\,'(\vec{r};t)] + \vec{q}\,'(\vec{r};t) \approx \mu\nabla^2 \vec{s}\,'(\vec{r};t) + \vec{q}\,'(\vec{r};t) \qquad , \qquad (4)$$

$$\Rightarrow \nabla^2 \vec{s}\,'(\vec{r};t) - \frac{1}{\mu/\rho(\vec{r};t)}\frac{\partial^2 \vec{s}\,'(\vec{r};t)}{\partial t^2} = -\frac{\vec{q}\,'(\vec{r};t)}{\mu} \Rightarrow \nabla^2 \vec{s}\,'(\vec{r};t) - \frac{1}{c_s^2(\vec{r};t)}\frac{\partial^2 \vec{s}\,'(\vec{r};t)}{\partial t^2} = -\frac{\vec{q}\,'(\vec{r};t)}{\mu}$$

where $c_s(\vec{r};t) = \sqrt{\mu/\rho(\vec{r};t)}$ is the shear wave speed, the subscript "s" means shear wave, and $\nabla \cdot \vec{s}\,'(\vec{r};t) \approx 0$ due to incompressibility of the media such as biological soft tissues. In cylindrical coordinates, Eq. (4) is given by:

$$\left[\frac{1}{r_0}\frac{\partial}{\partial r_0}(r_0\frac{\partial}{\partial r_0}) + \frac{1}{r_0^2}\frac{\partial^2}{\partial \phi_0^2} + \frac{\partial^2}{\partial z^2} - \frac{1}{c_s^2(\vec{r};t)}\frac{\partial^2}{\partial t^2}\right]\vec{s}(r_0,\phi_0,z;t) = -\frac{\vec{q}(r_0,\phi_0,z;t)}{\mu}, \qquad (5)$$

where $\vec{s}(r_0,\phi_0,z;t) = \vec{s}\,'(\vec{r};t)$, $\vec{q}(r_0,\phi_0,z;t) = \vec{q}\,'(\vec{r};t)$, $r_0 = \sqrt{x_0^2 + y_0^2}$ is the radial distance, ϕ_0 is the azimuthal angle, $x_0 = r_0\cos(\phi_0)$, $y_0 = r_0\sin(\phi_0)$, $\vec{r} = (r_0\cos(\phi_0), r_0\sin(\phi_0), z)$.
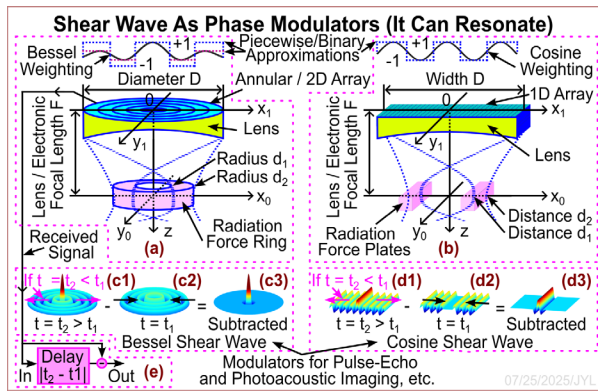

Fig. 1. Generation of shear waves for super-resolution imaging [15] via a phase modulation of the point spread function (PSF) of imaging systems such as pulse-echo and photoacoustic imaging [23]. (a) A cylindrical ring of radiation force produced near the focal distance by a focused Bessel beam (or its piecewise or binary approximation) that is generated with an annular or a 2D array transducer to produce a focused shear wave. (b) The same as (a) except that two plates of radiation force are produced by a focused cosine beam [22] or its binary approximation that is generated by a 1D array transducer. (c1), (c2), and (c3) are propagating shear waves produced by the radiation force in (a) at two different times t_2 and t_1 (either $t_2, > t_1$ or $t_2, < t_1$), and their subtracted version, respectively, to reduce the sidelobes in the modulated imaging waves. (d1), (d2), and (d3) are the same as (c1), (c2), and (c3) respectively except that the cosine shear waves are produced by the linear array in (b). (e) A sensitive and high-dynamic range interferometer method that is applicable to both (a) and (b) to perform a subtraction or phase-difference detection of modulated imaging-waves [15].
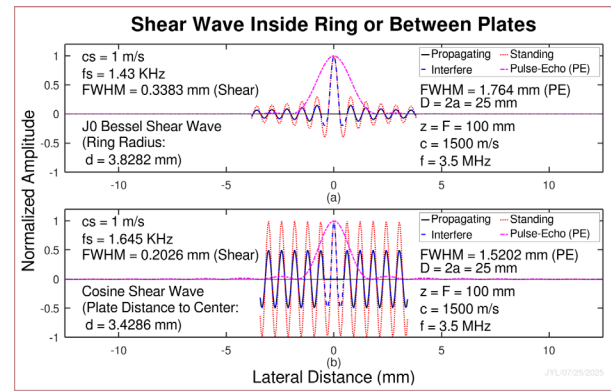
Fig. 2. Focused shear waves (attenuation not considered) to modulate imaging waves for super-resolution imaging (also see Figs. 1(c1)-1(c3) and 1(d1)-1(d3) for sidelobe reduction). (a) Results obtained with a focused Bessel beam transducer (annular or 2D array in Fig. 1(a)). (b) Results obtained with a focused cosine beam transducer (1D array in Fig. 1(b)). Solid lines (black) show propagating shear waves at a moment of time t_1 (no interference peak, see Figs. 1(c2) and 1(d2)). Dashed lines (blue) represent shear waves at another moment of time t_2 (with an interference peak, see Figs. 1(c1) and 1(d1)). Subtraction of solid from dashed lines results in an equivalent shear wave with a sharp peak but low-sidelobe. Dotted lines (red) are standing waves whose peak amplitudes depend on boundary conditions at d_1 and d_2 (Fig. 1) and shear-wave frequency ($d = (d_1+d_2)/2$ and (d_2-d_1) = FWHM (full-width-at-half-maximum) of the radiation force). Dash-dotted lines (pink) represent the pulse-echo (PE or two-way) PSF of the imaging system, and will be wider for photoacoustic imaging that uses one-way focusing. With the parameters given, image resolutions are 5.2 (a) and 7.5 (b) folds higher than the diffraction limits of the pulse-echo imaging using the shear-wave modulation method in Fig. 1.

B. SOLUTIONS TO THE WAVE EQUATION

I. SHEAR WAVE PRODUCED FROM CYLINDRICAL RING OR DISK OF RADIATION FORCE

a. Solutions to the Cylindrical Wave Equation without Fixed Boundaries:

Assuming that $c_s(\vec{r};t) = c_s$ is a constant (which means that $\rho(\vec{r};t)$ is a constant if μ is a constant), the shear wave displacement $\vec{s}(r_0, \phi_0, z; t)$ and the external volumetric force $\vec{q}(r_0, \phi_0, z; t)$ are not a function of both ϕ_0 and z, and these vectors have only the z component, i.e., $\vec{s}(r_0, \phi_0, z; t) = s(r_0, \phi_0, z; t)\vec{z}^0 = s(r_0;t)\vec{z}^0$ and $\vec{q}(r_0, \phi_0, z; t) = q(r_0, \phi_0, z; t)\vec{z}^0 = q(r_0;t)\vec{z}^0$, where $\vec{z}^0$ is a unit vector in z, Eq. (5) can be simplified (see Fig. 1(a)):

$$\left[\frac{1}{r_0}\frac{\partial}{\partial r_0}(r_0 \frac{\partial}{\partial r_0}) - \frac{1}{c_s^2}\frac{\partial^2}{\partial t^2} \right] s(r_0;t) = -\frac{q(r_0;t)}{\mu} . \tag{6}$$

If the external volumetric force is sinusoidal with frequency, f_s (angular frequency $\omega_s = 2\pi f_s$), i.e., $q(r_0;t) = Q(r_0)e^{-i\omega_s t}$ and $s(r_0;t) = S(r_0;\omega_s)e^{-i\omega_s t}$, where $i = \sqrt{-1}$, the subscript "s" of f_s and ω_s represents shear wave, and the amplitude of the volumetric force is uniform within the cylindrical ring, i.e., $Q(r_0) = Q_0$ is a constant for $0 \le d_1 \le r_0 \le d_2$, and $Q(r_0) = 0$ elsewhere, Eq. (6) becomes the following inhomogeneous Helmholtz equation:

$$\left[\frac{1}{r_0}\frac{\partial}{\partial r_0}\left(r_0 \frac{\partial}{\partial r_0} \right) - \frac{1}{c_s^2}\frac{\partial^2}{\partial t^2} \right] S(r_0;\omega_s)e^{-i\omega_s t} = -\frac{Q(r_0)e^{-i\omega_s t}}{\mu} \Rightarrow \frac{d^2 S(r_0;\omega_s)}{dr_0^2} + \frac{1}{r_0}\frac{dS(r_0;\omega_s)}{dr_0} + k_s^2 S(r_0;\omega_s) = \begin{cases} -\dfrac{Q_0}{\mu}, & 0 \le d_1 \le r_0 \le d_2 \\ 0, & \text{Otherwise} \end{cases}, \tag{7}$$

where d_1 and d_2 (see Fig. 1(a)) are the inner and outer radii of the cylindrical ring respectively, and $k_s = \omega_s / c_s$ is the wave number of the shear wave (k_s is a complex number if there is attenuation). General solutions to Eq. (7) can be obtained by getting a general solution to the homogeneous Helmholtz equation (setting the right hand side of Eq. (7) to zero) plus a specific solution to the inhomogeneous Helmholtz equation. Letting $\xi_0 = k_s r_0$ and $S(r_0;\omega_s) = S'(\xi_0;\omega_s)$, the homogeneous Helmholtz equation of Eq. (7) becomes a zeroth-order Bessel equation:

$$r_0^2 \frac{d^2 S(r_0;\omega_s)}{dr_0^2} + r_0 \frac{dS(r_0;\omega_s)}{dr_0} + k_s^2 r_0^2 S(r_0;\omega_s) = 0 \Rightarrow \xi_0^2 \frac{d^2 S'(\xi_0;\omega_s)}{d\xi_0^2} + \xi_0 \frac{dS'(\xi_0;\omega_s)}{d\xi_0} + \xi_0^2 S'(\xi_0;\omega_s) = 0 . \tag{8}$$

Thus, the general solutions to Eq. (7) are given by (see the standing wave or the red dotted line in Fig. 2(a)):

$$S(r_0;\omega_s) = S'(\xi_0;\omega_s) = \begin{cases} A_0 J_0(k_s r_0), & 0 \le r_0 \le d_1 \\ B_0 J_0(k_s r_0) + C_0 Y_0(k_s r_0) - Q_0 / (k_s^2 \mu), & d_1 < r_0 \le d_2 \\ D_0 H_0^{(1)}(k_s r_0), & r_0 > d_2 \end{cases}, \tag{9}$$

where $-Q_0 / (k_s^2 \mu)$ is a specific solution to Eq. (7) in the region $d_1 < r_0 \le d_2$, $J_0(k_s r_0)$ and $Y_0(k_s r_0)$ are the zeroth-order Bessel functions of the first and second kind respectively ($Y_0(k_s r_0)$ is also called zeroth-order Neumann function), and $H_0^{(1)}(k_s r_0) = J_0(k_s r_0) + iY_0(k_s r_0)$ is the zeroth-order Hankel function of the first kind for an outgoing wave since its asymptotic behavior is $H_0^{(1)}(k_s r_0) \to \sqrt{2/(\pi k_s r_0)}e^{i(k_s r_0 - \pi/4)}$ as $k_s r_0 \to \infty$. Note that the coefficient of $Y_0(k_s r_0)$ for $r_0 \le d_1$ is set to zero in Eq. (9) (i.e., $S(r_0;\omega_s) = A_0 J_0(k_s r_0)$) since $|Y_0(k_s r_0)| \to \infty$ as $r_0 \to 0$. As for $r_0 > d_2$, $H_0^{(1)}(k_s r_0)$ instead of $J_0(k_s r_0)$ and $Y_0(k_s r_0)$ is used because the latter two represent standing waves. (Note: that if $S(r_0;\omega_s)$ also depends on ϕ_0, removing z, Eq. (5) can be used and the solutions will include a combination of n th-order Bessel functions, where n is an integer, as in Eq. (A2.3) in Appendix A2: "Derivation of Eq. (12)".)

Since both the displacement and stress (proportional to the radial derivative of the displacement according to the Hooke's law in isotropic linear elastic media) at boundaries should be continuous, the coefficients of $A_0, B_0, C_0,$ and D_0 in Eq. (9) can be obtained as follows (see Appendix A1 "Derivation of Eq. (10)"):

$$\begin{cases} A_0 = [i\pi Q_0 / (2k_s\mu)][d_2 H_1^{(1)}(k_s d_2) - d_1 H_1^{(1)}(k_s d_1)] \\ B_0 = [i\pi Q_0 / (2k_s\mu)][-d_1 J_1(k_s d_1) + d_2 H_1^{(1)}(k_s d_2)] \\ C_0 = [\pi Q_0 / (2k_s\mu)]d_1 J_1(k_s d_1) \\ D_0 = [i\pi Q_0 / (2k_s\mu)][-d_1 J_1(k_s d_1) + d_2 J_1(k_s d_2)] \end{cases}; \text{ and, in special case, } d_1 = 0, \text{ we have: } \begin{cases} A_0 = [i\pi Q_0 / (2k_s\mu)]d_2 H_1^{(1)}(k_s d_2) \\ B_0 = A_0 \\ C_0 = 0 \\ D_0 = [i\pi Q_0 / (2k_s\mu)]d_2 J_1(k_s d_2) \end{cases}. \tag{10}$$

If $d_1 = 0$ (see Eq. (10)), the shear wave is produced by a disk of radiation force and is given by:

$$S(r_0;\omega_s) = \begin{cases} B_0 J_0(k_s r_0) - Q_0 / (k_s^2 \mu) = [i\pi Q_0 / (2k_s\mu)]d_2 H_1^{(1)}(k_s d_2) J_0(k_s r_0) - Q_0 / (k_s^2 \mu), & 0 \le r_0 \le d_2 \\ D_0 H_0^{(1)}(k_s r_0) = [i\pi Q_0 / (2k_s\mu)]d_2 J_1(k_s d_2) H_0^{(1)}(k_s r_0), & r_0 > d_2 \end{cases}. \tag{11}$$

Alternatively, the solutions to Eq. (7) can be obtained with the Green's function method (see $G(r_0, r'; \omega_s)$ in Eq. (A2.2)) and the coefficients A_0' and D_0' in Eq. (A2.5), see Appendix A2 "Derivation of Eq. (12)" [28].

$$S(r_0;\omega_s) = 2\pi \int_{d_1}^{d_2} \frac{Q(r')}{\mu} G(r_0,r';\omega_s) r' dr' = \begin{cases} \dfrac{i\pi}{2\mu}\left[\displaystyle\int_{d_1}^{d_2} Q_0 H_0^{(1)}(k_s r') r' dr'\right] J_0(k_s r_0), & 0 \le r_0 \le d_1 \\[2ex] \dfrac{i\pi}{2\mu}\left\{\left[\displaystyle\int_{d_1}^{r_0} Q_0 J_0(k_s r') r' dr'\right] H_0^{(1)}(k_s r_0) + \left[\displaystyle\int_{r_0}^{d_2} Q_0 H_0^{(1)}(k_s r') r' dr'\right] J_0(k_s r_0)\right\}, & d_1 < r_0 \le d_2 \\[2ex] \dfrac{i\pi}{2\mu}\left[\displaystyle\int_{d_1}^{d_2} Q_0 J_0(k_s r') r' dr'\right] H_0^{(1)}(k_s r_0), & r_0 > d_2 \end{cases} \tag{12}$$

It can be proved that Eq. (12) is exactly the same as Eq. (9) since $\int H_0^{(1)}(x) x\, dx = x H_1^{(1)}(x)$ and $\int J_0(x) x\, dx = x J_1(x)$. However, unlike Eq. (9), Eq. (12) is more general since $Q(r_0)$ in Eq. (7) can be any well-behaved function within the ring $0 \le d_1 \le r_0 \le d_2$, which is the case for a remotely generated radiation force, although more computations are needed to calculate the integrations in Eq. (12) if $Q(r')$ is not a constant.

b.   Solutions with Fixed Shear-Wave Amplitude or Stress at the Boundary of a Cylindrical Ring:

Assuming that a cylindrical ring has a radius $d_1 > 0$ and is vibrating uniformly along z axis at a single frequency with a fixed amplitude A. According to Eq. (9), the shear wave produced inside the ring is given by:

$$S(r_0;\omega_s) = A_0'' J_0(k_s r_0), \quad 0 \le r_0 \le d_1, \tag{13}$$

where A_0'' is a coefficient to be determined with a fix-amplitude boundary condition (i.e., $S(r_0;\omega_s) = A$ at d_1):

$$A_0'' J_0(k_s d_1) = A \Rightarrow A_0'' = \frac{A}{J_0(k_s d_1)} \Rightarrow S(r_0;\omega_s) = \frac{A}{J_0(k_s d_1)} J_0(k_s r_0). \tag{14}$$

If at the boundary d_1, a harmonic shear stress is uniformly applied along the z axis with a fixed magnitude T_{d_1}, using Eq. (13), the boundary condition and the resulting shear wave inside the ring is given by:

$$\mu \frac{dS(r_0;\omega_s)}{dr_0}\bigg|_{r_0=d_1} = T_{d_1} \Rightarrow \mu[-A_0'' k_s J_1(k_s d_1)] = T_{d_1} \Rightarrow A_0'' = -\frac{T_{d_1}}{\mu k_s J_1(k_s d_1)} \Rightarrow S(r_0;\omega_s) = -\frac{T_{d_1}}{\mu k_s J_1(k_s d_1)} J_0(k_s r_0). \tag{15}$$
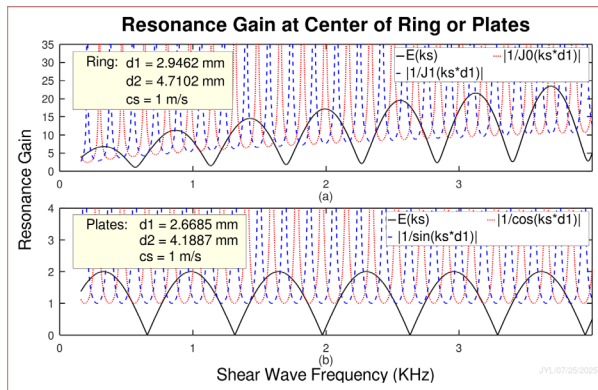
Fig. 3. Resonance gains of shear waves over frequency (no attenuation). (a) Resonance gain of the shear wave produced by a cylindrical ring of radiation force (see Fig. 1(a)). (b) Resonance gain of the shear wave produced by two plates of radiation force (see Fig. 1(b)). Solid lines (black) are the results obtained with continuity boundary conditions at both d_1 and d_2 (Fig. 1). Dotted (red) and dashed (blue) lines are resonance gains of the shear waves produced with a constant amplitude and shear stress at the boundary d_1 respectively, and they can be infinity at some frequencies. A large resonance gain increases the SNR of imaging systems. The parameters used are given in the figure.

c.   Resonance Gain:

The shear wave in free space (no resonance) for Eq. (7) can be obtained by getting a particular solution to Eq. (7) but without the boundaries at d_1 and d_2 (i.e., $Q(r_0) \equiv Q_0$ for all r_0):

$$S_{ref}(r_0;\omega_s) = -Q_0/(k_s^2 \mu), \tag{16}$$

where the subscript "*ref*" means "reference". The resonance gain of the shear wave at $r_0 = 0$ is given by [29]:

$$E(k_s) = \left| S(r_0; \omega_s) / S_{ref}(r_0; \omega_s) \right|_{r_0=0}, \tag{17}$$

which is a ratio between the magnitude of the shear wave (see Eqs. (9), (10), and (12)) produced by a cylindrical ring of external force and the magnitude of the reference shear wave in Eq. (16) at the center of the ring. Note that the reference shear waves for Eqs. (14) and (15) are $S_{ref}(r_0; \omega_s) = A$ and $-T_{d_1}/(\mu k_s)$ respectively. Plots of $E(k_s)$ versus $f_s = k_s c_s /(2\pi)$ are given in Fig. 3(a) (see black, red, and blue lines for Eqs. (9), (14), and (15), respectively).

II. SHEAR WAVE PRODUCED FROM TWO PARALLEL PLATES OF RADIATION FORCE

If the cylindrical ring of radiation force in Fig. 1(a) is replaced with two infinitely large parallel plates located symmetrically about $x_0 = 0$ (see Fig. 1(b)), Eq. (4) becomes a 1D equation that can be used to describe shear waves produced by a cosine-weighted 1D array transducer commonly used in medical ultrasound imaging systems:

$$\left[\frac{\partial^2}{\partial x_0^2} - \frac{1}{c_s^2(x_0;t)} \frac{\partial^2}{\partial t^2} \right] \vec{s}\,'(x_0;t) = -\frac{\vec{q}\,'(x_0;t)}{\mu}. \tag{18}$$

Assuming that $\vec{s}\,'(x_0;t) = s'(x_0;t)\vec{z}^0 = S(x_0;\omega_s)e^{-i\omega_s t}\vec{z}^0$, $\vec{q}\,'(x_0;t) = q'(x_0;t)\vec{z}^0 = Q(x_0)e^{-i\omega_s t}\vec{z}^0$, $c_s(x_0;t) = c_s$ is a constant, $k_s = \omega_s / c_s$, where $Q(x_0) = Q_0$ is a constant for $0 \leq d_1 \leq |x_0| \leq d_2$, and $Q(x_0) = 0$ elsewhere, Eq. (7) becomes a 1D inhomogeneous Helmholtz equation:

$$\frac{d^2 S(x_0;\omega_s)}{dx_0^2} + k_s^2 S(x_0;\omega_s) = \begin{cases} -\dfrac{Q_0}{\mu}, & 0 \leq d_1 \leq |x_0| \leq d_2 \\ 0, & \text{Otherwise} \end{cases}. \tag{19}$$

Similar to Eq. (9), the solutions (see the red dotted line in Fig. 2(b)) to Eq. (19) can be obtained using a general solution to the homogeneous Helmholtz equation plus a specific solution to the inhomogeneous Helmholtz equation:

$$S(x_0;\omega_s) = \begin{cases} (A_0'''/2)e^{ik_s x_0} + (A_0'''/2)e^{-ik_s x_0} = A_0'''\cos(k_s x_0), & -d_1 \leq x_0 \leq d_1 \\ B_0'''e^{ik_s x_0} + C_0'''e^{-ik_s x_0} - Q_0/(k_s^2 \mu), & 0 \leq d_1 < x_0 \leq d_2 \text{ or } -d_2 \leq x_0 < -d_1, \\ D_0'''e^{ik_s x_0}, & x_0 < -d_2 \text{ or } x_0 > d_2 \end{cases} \tag{20}$$

where the first row represents a standing shear wave formed between the plates ($-d_1 \leq x_0 \leq d_1$) by two plane waves propagating in opposite directions (see Fig. 1(b)).

Applying the boundary conditions of continuity of displacement and stress to Eq. (20), we have:

$$\begin{cases} (1) \text{ At } x_0 = d_1 \text{ (Displacement Continuity):} & A_0'''\cos(k_s d_1) = B_0'''e^{ik_s d_1} + C_0'''e^{-ik_s d_1} - Q_0/(k_s^2 \mu) \\ (2) \text{ At } x_0 = d_1 \text{ (Stress Continuity):} & d[A_0'''\cos(k_s x_0)]/dx_0 |_{x_0=d_1} = d[B_0'''e^{ik_s x_0} + C_0'''e^{-ik_s x_0}]/dx_0 |_{x_0=d_1} \\ (3) \text{ At } x_0 = d_2 \text{ (Displacement Continuity):} & B_0'''e^{ik_s d_2} + C_0'''e^{-ik_s d_2} - Q_0/(k_s^2 \mu) = D_0'''e^{ik_s d_2} \\ (4) \text{ At } x_0 = d_2 \text{ (Stress Continuity):} & d[B_0'''e^{ik_s x_0} + C_0'''e^{-ik_s x_0}]/dx_0 |_{x_0=d_2} = d[D_0'''e^{ik_s x_0}]/dx_0 |_{x_0=d_2} \end{cases}$$

$$\Rightarrow (1) \; A_0'''\cos(k_s d_1) - B_0'''e^{ik_s d_1} - C_0'''e^{-ik_s d_1} = -Q_0/(k_s^2\mu); \quad (2) \; -A_0'''\sin(k_s d_1) - iB_0'''e^{ik_s d_1} + iC_0'''e^{-ik_s d_1} = 0; \quad \tag{21}$$
$$(3) \; B_0'''e^{ik_s d_2} + C_0'''e^{-ik_s d_2} - D_0'''e^{ik_s d_2} = Q_0/(k_s^2\mu); \quad (4) \; B_0'''e^{ik_s d_2} - C_0'''e^{-ik_s d_2} - D_0'''e^{ik_s d_2} = 0$$

Solving Eq. (21), we obtain the coefficients A_0''', B_0''', C_0''', and D_0''' of the shear wave in Eq. (20):

$$A_0''' = [Q_0/(2k_s^2\mu)](2e^{ik_s d_2} - 2e^{ik_s d_1}); \quad B_0''' = [Q_0/(2k_s^2\mu)][-2i\sin(k_s d_1) + e^{ik_s d_2}]$$
$$C_0''' = [Q_0/(2k_s^2\mu)]e^{ik_s d_2}; \quad D_0''' = [Q_0/(2k_s^2\mu)][2i\sin(k_s d_2) - 2i\sin(k_s d_1)]. \tag{22}$$

Similar to Eqs. (14) and (15), if at the boundary $d_1 > 0$, the shear wave amplitude A and the stress amplitude T_{d_1} in the z direction are constant, the shear waves between the two plates are given by

$$S(d_1;\omega_s) = A_0'''\cos(k_s d_1) = A \Rightarrow A_0''' = \frac{A}{\cos(k_s d_1)} \Rightarrow S(x_0;\omega_s) = \frac{A}{\cos(k_s d_1)}\cos(k_s x_0) \tag{23}$$

and

$$\mu \frac{dS(x_0;\omega_s)}{dx_0}\bigg|_{x_0=d_1} = T_{d_1} \Rightarrow \mu[-A_0{'''}k_s\sin(k_sd_1)] = T_{d_1} \Rightarrow A_0{'''} = -\frac{T_{d_1}}{\mu k_s\sin(k_sd_1)} \Rightarrow S(x_0;\omega_s) = -\frac{T_{d_1}}{\mu k_s\sin(k_sd_1)}\cos(k_sx_0), \quad (24)$$

respectively, corresponding to the resonance gains (see Eq. (17)) of $|1/\cos(k_sd_1)|$ (normalized to A, see red dotted line in Fig. 3(b)) and $|1/\sin(k_sd_1)|$ (normalized to $-T_{d_1}/(\mu k_s)$, see blue dashed line in Fig. 3(b)).

C. RADIATION FORCES

a. Radiation Force Produced by a Focused Bessel Transducer at Its Focal Distance:

Below we will show how to produce a ring of radiation force for generation of a focused shear wave. Under paraxial condition, i.e., $r_0 \ll a$ (see Eqs. (31) and (32) of Ref. [21]), the ultrasound wave (longitudinal) pressure (the square of its magnitude is proportional to the radiation force [25]) produced by a focused transducer (radius a) weighted with an nth-order Bessel function $J_n(\alpha r_1)e^{in\phi_1}$, where $\alpha \geq 0$ is the scaling parameter, $r_1 = \sqrt{x_1^2+y_1^2}$ is the radial distance of a point (x_1,y_1) on the transducer aperture (Fig. 1(a)), and $\phi_1 = \tan^{-1}(y_1/x_1)$, is given by:

$$\tilde{\Phi}_{B_n}(x_0,y_0,z=F;\omega) = \frac{e^{ikF}}{i\lambda F}\left(1+\frac{i\lambda}{2\pi F}\right)e^{i\frac{k}{2F}r_0^2}(2\pi i^{-n}e^{in\phi_0})\mathcal{H}_n\{J_n(\alpha r_1)\}(k_0), \quad (25)$$

where the subscript "B_n" means nth-order Bessel beam, n is an integer, F is the focal distance, $\omega = 2\pi f$ is an angular frequency, f is the frequency, $k = \omega/c = 2\pi/\lambda$ is the wavenumber, λ is the wavelength, c is the speed of sound, $k_0 = kr_0/F$, r_0 is the radial distance at F (see Fig. 1(a)), ϕ_0 is an azimuthal angle, and $\mathcal{H}_n\{J_n(\alpha r_1)\}(k_0)$ is a Hankel transform of $J_n(\alpha r_1)$ (see Eq. (32) of Ref. [21], P. 619 of Ref. [30], and P. 664 of Ref. [31]):

$$\mathcal{H}_n\{J_n(\alpha r_1)\}(k_0) = \int_0^a \{J_n(\alpha r_1)\}J_n(k_0r_1)r_1dr_1 = \begin{cases} a^2\dfrac{(\alpha a)J_n(k_0a)J_{n+1}(\alpha a)-(k_0a)J_n(\alpha a)J_{n+1}(k_0a)}{(\alpha a)^2-(k_0a)^2}, & k_0 \neq \alpha \\[2mm] a^2\dfrac{(\alpha a)[J_n^2(\alpha a)+J_{n+1}^2(\alpha a)]-2nJ_n(\alpha a)J_{n+1}(\alpha a)}{2(\alpha a)}, & k_0 = \alpha \end{cases} \quad (26)$$

(where $n = -\infty,\cdots,-1,0,1,\cdots,\infty$)

At $k_0 = \alpha$, there is a major peak in Eq. (26) (see Figs. 4(a) and 5(a)), which means that the sound pressure produced by a focused Bessel transducer is a cylindrical ring of a radius of $r_0 = \alpha F/k$ and the ring thickness becomes zero as $a \to \infty$ (Eqs. (31) and (32) of Ref. [21], P. 943 of Ref. [30], and P. 661 of Ref. [31]). If $n=0$, Eq. (26) becomes:

$$\mathcal{H}_0\{J_0(\alpha r_1)\}(k_0) = \begin{cases} a^2\dfrac{(\alpha a)J_0(k_0a)J_1(\alpha a)-(k_0a)J_0(\alpha a)J_1(k_0a)}{(\alpha a)^2-(k_0a)^2}, & k_0 \neq \alpha \\[2mm] a^2\dfrac{J_0^2(\alpha a)+J_1^2(\alpha a)}{2}, & k_0 = \alpha \\[2mm] a^2\dfrac{1}{2}\mathrm{Jinc}(\alpha a), & k_0 = 0 \\[2mm] \approx a^2\dfrac{J_0(\alpha a)}{2}\left[\dfrac{2J_1(k_0a)}{(k_0a)}\right] = a^2\dfrac{J_0(\alpha a)}{2}\mathrm{Jinc}(k_0a), & k_0 \gg \alpha \text{ and } J_0(\alpha a) \neq 0 \end{cases} \quad (27)$$

where $\mathrm{Jinc}(\cdot)$ is a jinc function (defined as $\mathrm{Jinc}(x) = 2J_1(x)/x$ with x as an argument). For simplicity, we assume that the profile of the major peak (see Fig. 4(a), plotted along a ring diameter) is approximately a jinc function that is the beam profile of a focused plane wave (setting $\alpha = 0$ in Eqs. (25) and (27)) produced by a disk transducer of a radius a at its focal distance (see Eqs. (35) and (36) of Ref. [21], and Eqs. 2-35 and 4-31 of Ref. [28]), i.e.:

$$\tilde{\Phi}_P(x_0,y_0,z=F;\omega) = \frac{e^{ikF}}{i\lambda F}\left(1+\frac{i\lambda}{2\pi F}\right)e^{i\frac{k}{2F}r_0^2}[\pi a^2\,\mathrm{Jinc}(k_0a)], \quad (28)$$

where the subscript "P" means "plane wave", and its intensity is given by the pink dash-dotted line in Fig. 2(a).

b. Radiation Force Produced by a Focused Cosine Transducer at Its Focal Distance:

The longitudinal ultrasound wave pressure at the focal distance F of a focused beam produced by a transducer located at the plane $z = 0$ in rectangular coordinates is given by (see Eq. (28) of Ref. [21], Eq. 5-14 of Ref. [28]):

$$\tilde{\Phi}(x_0, y_0, z = F; \omega) = \frac{e^{ikz}}{i\lambda F} e^{i\frac{k}{2F}(x_0^2+y_0^2)} \int_{-\infty}^{\infty}\int_{-\infty}^{\infty} [\tilde{\Phi}'_1(x_1, y_1; \omega)] e^{-i(k_{x_0}x_1+k_{y_0}y_1)} dx_1 dy_1 = \frac{e^{ikF}}{i\lambda F}\left(1+\frac{i\lambda}{2\pi F}\right) e^{i\frac{k}{2F}(x_0^2+y_0^2)} \mathcal{F}_{x_1,y_1}\{\tilde{\Phi}'_1(x_1, y_1; \omega)\}(k_{x_0}, k_{y_0}) , \quad (29)$$

where $k_{x_0} = kx_0/F$, $k_{y_0} = ky_0/F$, $\tilde{\Phi}'_1(x_1, y_1; \omega)$ is the weighting function at the transducer aperture on the coordinates (x_1, y_1) before a physical lens or an electronic focusing is applied, and $\mathcal{F}_{x_1,y_1}\{\}$ is a 2D Fourier transform in terms of x_1 and y_1. If the transducer is one dimensional (uniform over the elevation dimension y_1) and is weighted with a cosine function $\cos(\alpha x_1)$ (see Fig. 1(b)), where $\alpha \geq 0$ is the scaling parameter, the ultrasound beam (used to obtain radiation force) at the focal distance is given by the following 1D Fourier transform:

$$\tilde{\Phi}(x_0, z = F; \omega) = \frac{e^{ikF}}{i\lambda F}\left(1+\frac{i\lambda}{2\pi F}\right) e^{i\frac{k}{2F}x_0^2} \int_{-a}^{a} \cos(\alpha x_1) e^{-ik_{x_0}x_1} dx_1 = \frac{e^{ikF}}{i\lambda F}\left(1+\frac{i\lambda}{2\pi F}\right) e^{i\frac{k}{2F}x_0^2} \int_{-a}^{a} \frac{e^{i\alpha x_1}+e^{-i\alpha x_1}}{2} e^{-ik_{x_0}x_1} dx_1$$

$$= \frac{e^{ikF}}{i\lambda F}\left(1+\frac{i\lambda}{2\pi F}\right) e^{i\frac{k}{2F}x_0^2}\begin{cases} \dfrac{(k_{x_0}+\alpha)\sin[(k_{x_0}-\alpha)a]+(k_{x_0}-\alpha)\sin[(k_{x_0}+\alpha)a]}{k_{x_0}^2-\alpha^2} = a\{\text{sinc}[(k_{x_0}-\alpha)a]+\text{sinc}[(k_{x_0}+\alpha)a]\}, & k_{x_0} \neq \alpha \\[2ex] \dfrac{2\alpha a+\sin(2\alpha a)}{2\alpha} = a[1+\text{sinc}(2\alpha a)], & k_{x_0} = \pm\alpha \\[2ex] 2a\,\text{sinc}(\alpha a), & k_{x_0} = 0 \end{cases}, \quad (30)$$

where a is the half width of the transducer along the x_1 direction and $\text{sinc}(x) = \sin(x)/x$ is the sinc function. Eq. (30) has two peaks at $k_{x_0} = \pm\alpha$ or $x_0 = \pm F\alpha/k$, which are symmetric about the $x_0 = 0$ (see Fig. 4(b)). If $\alpha = 0$, we obtain focused plane wave at the focal distance of a 1D array transducer:

$$\tilde{\Phi}(x_0, z = F; \omega) = \frac{e^{ikF}}{i\lambda F}\left(1+\frac{i\lambda}{2\pi F}\right) e^{i\frac{k}{2F}x_0^2} \int_{-a}^{a} e^{-ik_{x_0}x_1} dx_1 = \frac{e^{ikF}}{i\lambda F}\left(1+\frac{i\lambda}{2\pi F}\right) e^{i\frac{k}{2F}x_0^2} [2a\,\text{sinc}(k_{x_0}a)] , \quad (31)$$

which is proportional to the sinc function, and its intensity is given by the pink dash-dotted line in Fig. 2(b).
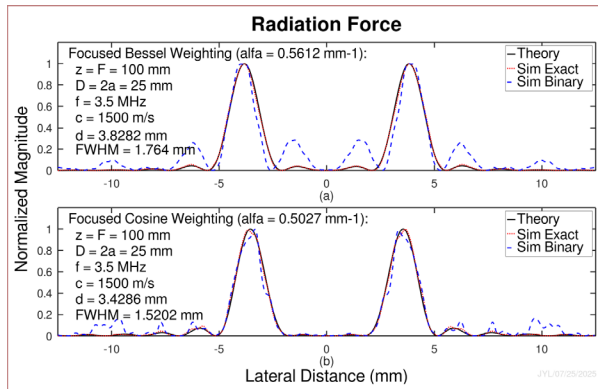

Fig. 4. Radiation forces produced by (a) a focused Bessel beam transducer (see Fig. 1(a)) and (b) a focused cosine beam transducer (see Fig. 1(b)) at the focal distance. Solid lines (black) were obtained theoretically with the Rayleigh-Sommerfeld diffraction formula. Dotted lines (red) are the results of computer simulations with an exact Bessel or cosine aperture weighting. Dashed lines (blue) are the same as the dotted lines except that a piecewise (binary) aperture weighting was used to increase transmit power. The parameters used are shown in the figure. An experiment result of the radiation force using a focused Bessel beam can be found in [32].
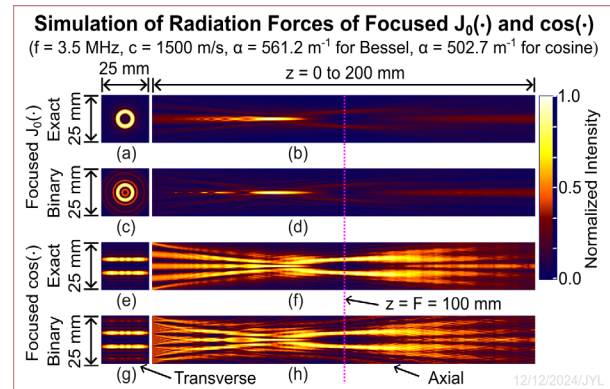

Fig. 5. Simulated radiation forces with the same parameters as those in Fig. 4. (a) and (b) are transverse (x_0-y_0 plane at $z = F = 100$ mm, see the vertical pink line) and axial (x_0-z plane from $z = 0$ to 200 mm) profiles, respectively, of the radiation forces produced by a focused Bessel transducer (see Fig. 1(a)) with an exact Bessel aperture weighting. (c) and (d) are the same as (a) and (b) respectively except that a piecewise (binary) aperture weighting is used to increase transmit power. (e) to (h) are the same as (a) to (d) respectively except that a focused cosine transducer (see Fig. 1(b)) is used. The color bar shows normalized beam intensity or radiation force.

3. RESULTS AND DISCUSSION

Super-Resolution Imaging and Sidelobe Reduction: The principle and details of the PSF-modulation super-resolution (breaking the diffraction limit) imaging method using amplitude, phase, or their combination are given in Ref. [15], where the modulator can be, for example, a nanoparticle, a small wave emitter, and a shear wave. Since the method is based on the LSI system theory and many practical imaging systems are LSI, in principle, the method can be applied to various disciplines of science, engineering, and medicine [15]-[18]. Fig. 1 shows implementations of the PSF-modulation super-resolution imaging method using shear waves (also see Figs. 8 and 9 of Ref. [15]).

In Fig. 1(a), a focused annular (or 2D) array transducer (diameter $D = 2a$, center frequency f, speed of sound c, wave length $\lambda = c/f$, wavenumber $k = 2\pi/\lambda$, and focal length F realized with a lens or electronic focusing) is weighted on its aperture (see the $x_1 - y_1$ coordinates and Eqs. (25) and (27)) with a Bessel function (or its piecewise or binary approximation [19]) to produce a cylindrical ring of sinusoidal radiation force (inner and outer diameters of d_1 and d_2 of the ring respectively) near the focal distance (at the $x_0 - y_0$ plane with a scaled radial distance of $k_0 = kr_0/F$). The cylindrical ring of radiation force produces a standing shear wave $A_0 J_0(k_s r_0)$ focused inside the ring ($0 \le r_0 \le d_1$, see Eq. (9) or (12), with frequency f_s, wave speed c_s, and wavenumber $k_s = 2\pi f_s/c_s$, where the subscript "s" means "shear wave"). The shear wave is then used to remotely modulate the phase of the imaging waves (such as the conventional focused beams of pulse-echo, photoacoustic, and NDE imaging systems) for super-resolution imaging of the mechanical properties (related to shear wave amplitude, attenuation, speed, spectrum, and nonlinearity) of objects (such as biological soft tissues) if the half wavelength (λ_s) of the shear wave is smaller than the size of the PSF of the imaging systems (see Eq. (28)). Note that the standing shear wave in Eq. (9) (or Eq. (12)) has high sidelobes, which may lower the image contrast. Since the standing wave is formed by a propagating wave (see the snapshots at two moments of times, t_2 in Fig. 1(c1) and t_1 in Fig. 1(c2), where $|t_2 - t_1| = T_s = 1/f_s$, T_s is the shear wave period, and an interference peak is formed at t_2), to reduce sidelobes, the shear waves at the two moments of time can be used to modulate the phases of two imaging waves respectively. Subtracting or detecting the phase difference between the two modulated imaging waves (motion effects can be neglected since usually $T_s < 1$ ms), a pixel of super-resolution image can be reconstructed with an equivalent shear wave that has a sharp interference peak and low sidelobes (see Figs. 1(c3)). Steering both the shear wave and the imaging waves from one spatial position to another and repeating the process above, a 2D or three-dimensional (3D) super-resolution image can be reconstructed (note that the beam produced by an annular array transducer can be steered mechanically with a reflector, see Figs. 7 and 8 of Ref. [20], and the beam of a 2D array transducer can be steered electronically). The sidelobe reduction method above can be implemented either when the propagating shear wave forms an interference peak at its center axis (i.e., $t_2 > t_1$) or when the peak of a standing shear wave is starting to disappear after the radiation force is turned off (i.e., $t_2 < t_1$). The procedure for super-resolution imaging with Fig. 1(b) and Figs. 1(d1)-1(d3) is the same as that with Fig. 1(a) and Figs. 1(c1)-1(c3), except that a 1D array transducer (along x_0 or $k_{x_0} = kx_0/F$) weighted with a cosine function (or its binary approximation) (see Eq. (30) [15][19][22]) is used to produce a propagating or a standing shear wave (Eq. (20)). The major advantage of using a 1D array transducer is that the method is easier to be implemented in existing commercial medical ultrasound imaging systems since most systems use 1D arrays.

Fig. 2(a) gives quantitative results of Figs. 1(a) and 1(c1)-1(c3) with parameters typically used in medical ultrasound imaging: $D = 25$ mm, $f = 3.5$ MHz, $F = 100$ mm, $c = 1500$ m/s, $\lambda = 0.4286$ mm, $k = 14.661$ mm^{-1}, $c_s = 1$ m/s, $f_s = 1.43$ KHz, the FWHM of the center peak of the standing shear-wave is equal to 0.3383-mm (see Eq. (9) (or Eq. (12)) and the red dotted line), $d_1 = 2.9462$ mm, $d_2 = 4.7102$ mm, $d = (d_1 + d_2)/2 = 3.8282$ mm, and the ring width $d_2 - d_1$ is approximately set to $PR^2_{FWHM} = 2r_0 \approx 1.029\lambda F/D = 1.764$ mm (see Eq. (28)), where PR^2_{FWHM} is the FWHM of $|\tilde{\Phi}_P(x_0, y_0, z = F; \omega)|^2$, $r_0 = 1.61633 F/(ka) = (1.61633/\pi)\lambda F/D$ because $\text{Jinc}^2(k_0 a) = \text{Jinc}^2(1.61633) = 0.5$, R_{FWHM} in PR^2_{FWHM} means the FWHM resolution, the superscript "2" means "squared", and the prefix P means focused "plane wave", as explained in the paragraph below Eq. (37) of Ref. [21]. The red dotted, black solid, blue dashed, and pink dash-dotted lines in Fig. 2(a) correspond to Eq. (9) (or Eq. (12)), Fig. 1(c2), Fig. 1(c1), and the pulse-echo (or PE) response of Eq. (28), respectively. Fig. 2(b) is the same as Fig. 2(a) except that $f_s = 1.645$ KHz, the FWHM of the center peak of the standing shear wave (see Eq. (20) and the red dotted line) is equal to 0.2026 mm, $d_1 = 2.6685$ mm, $d_2 = 4.1887$ mm, $d = 3.4286$ mm, and the plate width $d_2 - d_1$ is approximately set to $PR^2_{FWHM} = 2x_0 \approx 0.8868\lambda F/D = 1.5202$ mm, where $x_0 = 1.393 F/(ka) = 0.4434\lambda F/D$ because $\text{sinc}^2(k_{x_0} a) = \text{sinc}^2(1.393) = 0.5$, and PR^2_{FWHM} is the

pulse-echo (PE) response of Eq. (31). Note that in addition to the imaging method above, the standing shear wave in Eq. (20) (see the red dotted line in Fig. 2(b)) can be used directly to reconstruct super-resolution images with a computerized tomography (CT) method where each modulated imaging wave produces a projection and multiple projections can be obtained by rotating the 1D array transducer in Fig. 1(b). Using the parameters in Figs. 2(a) and 2(b), the image resolutions can be increased by 5.2 and 7.5 folds respectively beyond the diffraction limits given by Eqs. (28) and (31).

Shear-Wave Resonance: Fig. 3(a) shows a plot of the resonance gain $E(k_s)$ (see the black solid line and Eqs. (16) and (17)) versus the frequency f_s (related to k_s) of the shear wave (see Eq. (9) or (12)) produced by a cylindrical ring of radiation force (Fig. 1(a)) using the same parameters as those in Fig. 2(a). It is clear that the resonance gain (the black solid line in Fig. 3(a)) has peaks, i.e., the shear wave can resonate, and the values of the peaks increase with the shear-wave frequency (it also can be shown that the resonance gain increases with the ring radius d, and the distance between the peaks increase as the ring width $d_2 - d_1$ decreases). In a uniform media, if the radiation force could exert a localized oscillatory stress to form effective stiffness discontinuities and thus a partially reflective boundary, a Fabry–Perot type of resonance [33] can be established to further increase the resonance gain (for simplicity, the effective stiffness discontinuities, if there are any, have not been considered in Eq. (9) or Eq. (12)). The Fabry-Perot resonance can be established by locking the phase of the radiation force with the shear wave produced via a feedback mechanism [26]. A larger resonance gain will increase the shear-wave amplitude and thus boost the SNR and produce stronger nonlinear components in super-resolution imaging [15] (the nonlinearity created may help to distinguish benign tissues from malignant without biopsy). The red dotted and blue dashed lines in Fig. 3(a) are plots of the resonance gains of the shear waves produced with a fixed amplitude (see Eq. (14)) and stress (see Eq. (15)) respectively at the boundary d_1. In these cases, a strong Fabry–Perot–type resonance [33] is established and the resonance gains can be infinity at some shear-wave frequencies if there is no attenuation, i.e., $|1/J_0(k_s d_1)| \to \infty$ as $k_s d_1 \to 2.4048$, 5.5201, 8.6537, 11.7915, and 14.9309, $\cdots$, (red dotted line), and $|1/J_1(k_s d_1)| \to \infty$ as $k_s d_1 \to 0$, 3.8317, 7.0156, 10.1735, and 13.3237, $\cdots$, (blue dashed line) in Fig. 3(a). Fig. 3(b) is the same as Fig. 3(a) except that the shear waves are produced with a 1D array transducer in Fig. 1(b) using the same parameters as those in Fig. 2(b). Unlike Fig. 3(a), the maximum (resonant) and minimum (anti-resonant) of the resonance gain of the shear wave (see the black solid line and Eq. (20)) are 2 and 0 respectively, and the values of the peaks do not increase with the frequency. Similar to Fig. 3(a), under the conditions of a fixed amplitude (red dotted line and Eq. (23)) and stress (blue dashed line and Eq. (24)) at the boundary d_1, the resonance gains can be infinity at some frequencies, i.e., $|1/\cos(k_s d_1)| \to \infty$ as $k_s d_1 \to (2n+1)(\pi/2)$, $n = 0,1,2$, $\cdots$, (red dotted line), and $|1/\sin(k_s d_1)| \to \infty$ as $k_s d_1 \to n\pi$, $n = 0,1,2$, $\cdots$, (blue dashed line) in Fig. 3(b). Note that the resonating shear waves can be produced not only remotely, but also locally in applications such as NDE [24].

Radiation Forces: Fig. 4(a) shows radiation force (the body force $Q(r_0)$ in Eq. (7), proportional to the square of the module of the pressure) produced at the focal distance F of a focused Bessel transducer (see Fig. 1(a)) of scaling parameter α = $7.0156/a$ = 0.5612 mm^{-1} (α is chosen so that the radiation force on the axis is zero, i.e., $(a^2/2)\text{Jinc}(\alpha a) = 0$ at $k_0 = 0$ in Eq. (27)). The black solid, red dotted, and blue dashed lines in Fig. 4(a) are the results of theory (see Eqs. (25) and (27)), simulated (with C language in a Linux system) with an exact Bessel aperture weighting, and simulated with an approximated (binary) Bessel aperture weighting (i.e., $J_0(\alpha r_1) = 1$ if $J_0(\alpha r_1) \ge 0$, and $J_0(\alpha r_1) = -1$ otherwise [19]), respectively (using the same parameters as those in Figs. 2(a) and 3(a)). Fig. 4(b) (with the same parameters as those in Figs. 2(b) and 3(b)) is the same as Fig. 4(a) except that the radiation force ($Q(x_0)$ in Eq. (19)) is produced with a focused 1D cosine-weighted ($\cos(\alpha r_1)$) transducer in Fig. 1(b), where the scaling parameter α = $2\pi/a$ = 0.5027 mm^{-1} is chosen so that $2\text{sinc}(\alpha a) = 0$ at $k_{x_0} = 0$ in Eq. (30), $\cos(\alpha r_1) = 1$ if $\cos(\alpha r_1) \ge 0$, and $\cos(\alpha r_1) = -1$ otherwise (binary) [19][22]. It is clear that the simulated results (red dotted lines) in Fig. 4 are very close to those of the theory (black solid lines), indicating the accuracy of the simulation program. Note that there are multiple choices of the scaling parameter, α = $3.8317/a$, $7.0156/a$, $10.1735/a$, $13.3237/a$, and $16.4706/a$, $\cdots$, for Eq. (27), and $\alpha = n\pi/a$ ($n = 1,2,3$, $\cdots$) for Eq. (30), so that the radiation pressure on the center axis is zero. The specific choices of α in Fig. 4 are to minimize both the shear-wave propagation distance to reduce attenuation and an overlap of the radiation forces with the imaging waves. Once α is determined, $d = \alpha F/k$ in Figs. 2-4 can be calculated.

Figs. 5(a) and 5(b) are simulated transverse (in $x_0 - y_0$ plane at $F = 100$ mm, see the red dotted line in Fig. 4(a)) and axial (in $x_0 - z$ plane from $z = 0$ to 200 mm) profiles of a 3D radiation force produced by the transducer in Fig. 1(a). Since the cylindrical ring (Fig. 5(a)) of the radiation force has a large depth of field (about 25 mm, see Fig. 5(b)), a 2D ($x_0 - z$) super-resolution image can be reconstructed in real time by steering a 1D ultrasound beam along x_0. Fig. 5(c) (blue dashed line in Fig. 4(a)) and Fig. 5(d) are the same as Fig. 5(a) and Fig. 5(b) respectively, except that a binary approximation to the Bessel weighting is used. Figs. 5(e) to 5(h) are the same as Figs. 5(a) to 5(d) respectively except that

the transducer in Fig. 1(b) and the parameters in Fig. 4(b) are used. The benefits of the binary approximations (Figs. (4) and (5)) are to increase the transmit power while getting reasonably good cylindrical ring and plates of radiation forces.

Conventional Focused Beams: If $\alpha = 0$ in Eqs. (25) and (27), the focused Bessel beam in Fig. 1(a) becomes a conventional focused plane wave in Eq. (28), which means that conventional beams can be used the same way as the focused Bessel beam to produce a focused shear wave (see Eq. (11) that is a special case of Eq. (9) (or Eq. (12)) with $d_1 = 0$) to modulate the phase of imaging waves for super-resolution imaging, resulting in a new imaging approach that has not been exploited previously [4][11][25][34]. The benefits of using conventional focused beams are that the imaging systems can be simplified and the attenuation of shear wave can be minimized due to a shorter propagation distance of the wave, which means that a higher shear-wave frequency can be used to further increase image resolution while increasing image frame rate. Despite of the benefits, there may be a spatial overlap of the radiation force with both the shear wave and the imaging waves. However, since the overlap is the same from one spatial position to another in imaging, they can be removed from the super-resolution images with methods such as that given in Figs. 1(c1)-1(c3). Setting $\alpha = 0$ in Eqs. (29) and (30) , the focused cosine beam in Fig. 1(b) also becomes a conventional focused plane wave (see Eq. (31)). As is in the case of focused Bessel beam in Fig. 1(a), super-resolution images can be reconstructed with the shear wave that is obtained by setting $d_1 = 0$ in Eqs. (20) and (22) using the image reconstruction method in Figs. 1(d1)-1(d3).

Sensitivity and Dynamic Range: Finally, as shown in Figs. 1(c1)-1(c3) and Figs. 1(d1)-1(d3), super resolution images of low sidelobes can be reconstructed with a subtraction or detection of phase difference between two shear-wave modulated imaging waves. However, this requires the imaging system to have a large dynamic range and high sensitivity since a subtraction of two large signals can result in a small signal. Fig. 1(e) shows an approach that is applicable to both Figs. 1(a) and 1(b) and is similar to an optical interferometer to increase both dynamic range and sensitivity. In Fig. 1(e), imaging waves modulated at two moments of times t_1 and t_2 are scattered back from an object and then focused with a lens into a branched acoustic pipe using a modified transducer that allows waves to propagate both forward and backward, where the difference of the delay times between the two branches of the pipe is $| t_2 - t_1 | = T_s$ and the waves from the outputs of the branches are interfered before being converted to an electrical signal, amplified, and then digitized. If the modification of the transducer is not desired and one of the two electrical signals (modulated at t_1 and t_2) from the transducer can be delayed, the difference between the two signals can be obtained with an operational amplifier of a high common mode rejection rate to increase the dynamic range. Note that the modulator can be either a shear wave or a small physical particle. With an increased dynamic range and sensitivity in Fig. 1(e) (using an optical interferometer and optical fiber delay line), atomic optical imaging may be possible if small particles such as optically opaque ions that can be manipulated by an external electrical field are used as modulators (also see the descriptions on Page 167 of Ref. [15]).

4.CONCLUSION

Methods of producing modulators for low-sidelobe and high-contrast super-resolution imaging using focused shear waves generated remotely by a cylindrical ring (Fig. 1(a)), plates (Fig. 1(b)), or a disk/plate (with conventional focused beam in Eqs. (28) and (31)) of radiation forces were studied in details both theoretically and with computer simulations. These shear waves can resonate to form large peaks under certain boundary conditions to increase image SNR and help to assess object nonlinearity, and they also can be produced locally. If the modulated imaging waves can interfere directly before being detected (Fig. 1(e)), the sensitivity and dynamic range, and thus the image resolution can be greatly increased (an atomic optical imaging may thus be possible if small physical particles such as optically opaque ions are used as modulators). Because the cylindrical ring or plates of radiation forces have a larger depth of field (Fig. 5), real-time 2D super-resolution imaging with focused shear waves is possible. This study pays a way for super-resolution imaging of mechanical properties (shear-wave amplitude, speed, spectrum, and nonlinearity) of biological soft tissues deep in the body, which helps to distinguish between benign and malignant tissues, monitor therapies, and guide surgical operations.

5. APPENDICES

APPENDIX A1: DERIVATION OF EQ. (10) – COEFFICIENTS OF SHEAR WAVE IN EQ. (9)
Applying the continuity boundary conditions to Eq. (9), we obtain:

$$\begin{cases} (1) \ \text{At } r_0 = d_1 \ (\text{Displacement Continuity}): & A_0 J_0(k_s d_1) = B_0 J_0(k_s d_1) + C_0 Y_0(k_s d_1) - Q_0 /(k_s^2 \mu) \\ (2) \ \text{At } r_0 = d_1 \ (\text{Radial Stress Continuity}): & d[A_0 J_0(k_s r_0)] / dr_0 \, |_{r_0 = d_1} = d[B_0 J_0(k_s r_0) + C_0 Y_0(k_s r_0)] / dr_0 \, |_{r_0 = d_1} \\ (3) \ \text{At } r_0 = d_2 \ (\text{Displacement Continuity}): & B_0 J_0(k_s d_2) + C_0 Y_0(k_s d_2) - Q_0 /(k_s^2 \mu) = D_0 H_0^{(1)}(k_s d_2) \\ (4) \ \text{At } r_0 = d_2 \ (\text{Radial Stress Continuity}): & d[B_0 J_0(k_s r_0) + C_0 Y_0(k_s r_0)] / dr_0 \, |_{r_0 = d_2} = d[D_0 H_0^{(1)}(k_s r_0)] / dr_0 \, |_{r_0 = d_2} \end{cases} \quad . \quad \text{(A1.1)}$$

$\Rightarrow (1) \; A_0 J_0(k_s d_1) - B_0 J_0(k_s d_1) - C_0 Y_0(k_s d_1) = -Q_0/(k_s^2 \mu); \quad (2) \; A_0 J_1(k_s d_1) - B_0 J_1(k_s d_1) - C_0 Y_1(k_s d_1) = 0;$

$(3) \; B_0 J_0(k_s d_2) + C_0 Y_0(k_s d_2) - D_0 H_0^{(1)}(k_s d_2) = Q_0/(k_s^2 \mu); \quad (4) \; B_0 J_1(k_s d_2) + C_0 Y_1(k_s d_2) - D_0 H_1^{(1)}(k_s d_2) = 0$

Solving the system of 4 equations above, we obtain the coefficients $A_0, B_0, C_0,$ and D_0 in Eq. (10).

APPENDIX A2: DERIVATION OF EQ. (12) – SOLUTION VIA GREEN'S FUNCTION

Assuming that an external line source along the z direction is located at (x',y') point in rectangular (or (r',ϕ') in cylindrical) coordinates, which is represented by a Delta function (its dimension is an inverse of the argument) [35]:

$$\delta(x_0 - x', y_0 - y') = \delta(x_0 - x')\delta(y_0 - y') = \frac{\delta(r_0 - r')}{r_0}\delta(\phi_0 - \phi') = \frac{\delta(r_0 - r')}{r_0}\left[\frac{1}{2\pi}\sum_{n=-\infty}^{\infty} e^{in(\phi_0 - \phi')}\right], \quad (A2.1)$$

where the periodic function $\delta(\phi_0 - \phi')$ can be expanded as a Fourier series. Replacing Q_0/μ in Eq. (7) with Eq. (A2.1):

$$\left(\frac{\partial^2}{\partial r_0^2} + \frac{1}{r_0}\frac{\partial}{\partial r_0} + \frac{1}{r_0^2}\frac{\partial^2}{\partial \phi_0^2} + k_s^2\right)G(r_0, r'; \omega_s) = -\frac{\delta(r_0 - r')}{r_0}\left[\frac{1}{2\pi}\sum_{n=-\infty}^{\infty} e^{in(\phi_0 - \phi')}\right], \quad (A2.2)$$

where $G(r_0, r'; \omega_s)$ is the Green's function of Eq. (7) and also can be expanded as a Fourier series in terms of $\phi_0 - \phi'$:

$$\left(\frac{\partial^2}{\partial r_0^2} + \frac{1}{r_0}\frac{\partial}{\partial r_0} + \frac{1}{r_0^2}\frac{\partial^2}{\partial \phi_0^2} + k_s^2\right)\sum_{n=-\infty}^{\infty} g_n(r_0, r'; \omega_s)e^{in(\phi_0 - \phi')} = -\frac{\delta(r_0 - r')}{r_0}\left[\frac{1}{2\pi}\sum_{n=-\infty}^{\infty} e^{in(\phi_0 - \phi')}\right]$$

$$\Rightarrow \left[\frac{d^2}{dr_0^2} + \frac{1}{r_0}\frac{d}{dr_0} + \left(k_s^2 - \frac{n^2}{r_0^2}\right)\right]g_n(r_0, r'; \omega_s) = -\frac{\delta(r_0 - r')}{2\pi r_0}; \quad n = -\infty, \cdots, -1, 0, 1, \cdots, \infty \qquad , (A2.3)$$

$$\Rightarrow \text{When } r_0 \neq r', \text{the solution is: } g_n(r_0, r'; \omega_s) = g_n'(\xi_0, \xi'; \omega_s) = \begin{cases} A_n' J_n(k_s r_0), & r_0 < r' \\ D_n' H_n^{(1)}(k_s r_0), & r_0 > r' \end{cases}; \quad n = -\infty, \cdots, -1, 0, 1, \cdots, \infty$$

where n is the order of Bessel and Hankel functions. Superposing the first row of Eq. (A2.3) over the source, $Q(r_0)$:

$$\int_{d_1}^{d_2}\left\{\frac{Q(r')}{\mu}\left[\frac{d^2}{dr_0^2} + \frac{1}{r_0}\frac{d}{dr_0} + \left(k_s^2 - \frac{n^2}{r_0^2}\right)\right]\sum_{n=-\infty}^{\infty} g_n(r_0, r'; \omega_s)e^{in(\phi_0 - \phi')}\right\}r'dr' = -\int_{d_1}^{d_2}\left[\frac{Q(r')}{\mu}\frac{\delta(r_0 - r')}{r_0}\right]\left[\frac{1}{2\pi}\sum_{n=-\infty}^{\infty} e^{in(\phi_0 - \phi')}\right]r'dr'$$

$$\Rightarrow \left[\frac{d^2}{dr_0^2} + \frac{1}{r_0}\frac{d}{dr_0} + \left(k_s^2 - \frac{n^2}{r_0^2}\right)\right]\left[\sum_{n=-\infty}^{\infty}\int_{d_1}^{d_2}\frac{Q(r')}{\mu}g_n(r_0, r'; \omega_s)e^{in(\phi_0 - \phi')}r'dr'\right] = -\frac{Q(r_0)}{2\pi\mu}\sum_{n=-\infty}^{\infty} e^{in(\phi_0 - \phi')}$$

$$\Rightarrow \left(\frac{d^2}{dr_0^2} + \frac{1}{r_0}\frac{d}{dr_0} + k_s^2\right)\left[2\pi\int_{d_1}^{d_2}\frac{Q(r')}{\mu}g_0(r_0, r'; \omega_s)r'dr'\right] = -\frac{Q(r_0)}{\mu}; \quad \text{(when } n = 0\text{); compare with Eq. (7), we have:}$$

$$\Rightarrow S(r_0; \omega_s) = 2\pi\int_{d_1}^{d_2}\frac{Q(r')}{\mu}g_0(r_0, r'; \omega_s)r'dr' = 2\pi\int_{d_1}^{d_2}\frac{Q(r')}{\mu}G(r_0, r'; \omega_s)r'dr'; \quad \text{(when } n = 0\text{)} \text{ we obtain Eq.(12)}$$

where the Green's function $G(r_0, r'; \omega_s) = g_0(r_0, r'; \omega_s)$ (see Eqs. (A2.2) and (A2.3)) when $n = 0$, and A_0' and D_0' can be obtained by applying boundary conditions at r' to the second and the third rows of Eq. (A2.3) as follows:

(1) 1st Boundary Condition: $A_0' J_0(k_s r_0)|_{r_0 = r'} = D_0' H_0^{(1)}(k_s r_0)|_{r_0 = r'} \Rightarrow A_0' J_0(k_s r') - D_0' H_0^{(1)}(k_s r') = 0$

(2) 2nd Boundary Condition: $\lim_{\sigma \to 0}\int_{r'-\sigma}^{r'+\sigma}\left\{\frac{1}{r_0}\frac{d}{dr_0}\left[r_0\frac{dg_n(r_0, r'; \omega_s)}{dr_0}\right] + \left(k_s^2 - \frac{n^2}{r_0^2}\right)g_n(r_0, r'; \omega_s)\right\}r_0 dr_0 = \int_{r'-\sigma}^{r'+\sigma}\left[-\frac{\delta(r_0 - r')}{2\pi r_0}\right]r_0 dr_0$.(A2.5)

$$\Rightarrow \lim_{\sigma \to 0}\left\{\left[r_0\frac{dg_n(r_0, r'; \omega_s)}{dr_0}\right]\Big|_{r'-\sigma}^{r'+\sigma} + \lim_{\sigma \to 0}\int_{r'-\sigma}^{r'+\sigma}\left[\left(k_s^2 - \frac{n^2}{r_0^2}\right)g_n(r_0, r'; \omega_s)\right]r_0 dr_0\right\} = -\frac{1}{2\pi}; \quad \text{(Note: second lim is 0 due to 1st line)}$$

$$\Rightarrow \lim_{\sigma \to 0}\left\{D_n'\frac{d[H_n^{(1)}(k_s r_0)]}{dr_0}\Big|_{r'+\sigma} - A_n'\frac{d[J_n(k_s r_0)]}{dr_0}\Big|_{r'-\sigma}\right\} = -\frac{1}{2\pi r'}; \quad \text{(Note: stress jump is from } \delta\text{-function discontinuity)}$$

$$\Rightarrow -A_n'[J_{n-1}(k_s r') - J_{n+1}(k_s r')]/2 + D_n'[H_{n-1}^{(1)}(k_s r') - H_{n+1}^{(1)}(k_s r')]/2 = -1/(2\pi k_s r'); \quad n = -\infty, \cdots, -1, 0, 1, \cdots, \infty$$

$$\Rightarrow A_0' J_1(k_s r') - D_0' H_1^{(1)}(k_s r') = -1/(2\pi k_s r'); \quad \text{(when } n = 0\text{)} \Rightarrow \text{Solution: } \begin{cases} A_0' = (i/4)H_0^{(1)}(k_s r') \\ D_0' = (i/4)J_0(k_s r') \end{cases}$$

REFERENCES

[1] Ernst Abbe. "Beiträge zur Theorie des Mikroskops und der mikroskopischen Wahrnehmung." *Archiv für mikroskopische Anatomie* 9, no. 1 (1873): 413-468.

[2] B. Xu, Z. Wang, and J. He. "Super-resolution imaging via aperture modulation and intensity extrapolation." *Scientific reports* 8, no. 1 (2018): 15216.

[3] K. Gao, C. M. Donahue, B. G. Henderson, and R. T. Modrak. "SREMI: Super-resolution electromagnetic imaging with single-channel ground-penetrating radar." *Journal of Applied Geophysics* 205 (2022): 104777.

[4] G. Lerosey, J. De Rosny, A. Tourin, and M. Fink. "Focusing beyond the diffraction limit with far-field time reversal." *Science* 315, no. 5815 (2007): 1120-1122.

[5] R. Kumudham and V. Rajendran. "Super resolution enhancement of underwater sonar images." *SN Applied Sciences* 1, no. 8 (2019): 852.

[6] W. Chen, H. Jiang, and X. Huang. "Super-resolution acoustic imaging." *Applied Physics Letters* 120, no. 11 (2022).

[7] K. Prakash, B. Diederich, R. Heintzmann, and L. Schermelleh. "Super-resolution microscopy: a brief history and new avenues." *Philosophical Transactions of the Royal Society A* 380, no. 2220 (2022): 20210110.

[8] P. Song, J. M. Rubin, and M. R. Lowerison. "Super-resolution ultrasound microvascular imaging: Is it ready for clinical use?." *Zeitschrift für Medizinische Physik* (2023).

[9] K. Christensen-Jeffries, O. Couture, P. A. Dayton, Y. C. Eldar, K. Hynynen, F. Kiessling, M. O'Reilly, G. F. Pinton, G. Schmitz, M. Tang, M. Tanter, and R. J. G. van Sloun, "Super-resolution ultrasound imaging." *Ultrasound in medicine & biology* 46, no. 4 (2020): 865-891.

[10] O. Couture, V. Hingot, B. Heiles, P. Muleki-Seya, and M. Tanter. "Ultrasound localization microscopy and super-resolution: A state of the art." *IEEE transactions on ultrasonics, ferroelectrics, and frequency control* 65, no. 8 (2018): 1304-1320.

[11] M. Fink and M. Tanter. "Multiwave imaging and super resolution." *Physics today* 63, no. 2 (2010): 28-33.

[12] H. W. Jones, "Superresolution in ultrasonic imaging." *Acoustical Imaging* (1993): 71-76.

[13] S. W. Hell and J. Wichmann. "Breaking the diffraction resolution limit by stimulated emission: stimulated-emission-depletion fluorescence microscopy." *Optics letters* 19, no. 11 (1994): 780-782.

[14] E. Betzig, G. H. Patterson, R. Sougrat, O. W. Lindwasser, S. Olenych, J. S. Bonifacino, M. W. Davidson, J. Lippincott-Schwartz, and H. F. Hess. "Imaging intracellular fluorescent proteins at nanometer resolution." *science* 313, no. 5793 (2006): 1642-1645.

[15] Jian-yu Lu, " Modulation of point spread function for super-resolution imaging." *IEEE Transactions on Ultrasonics, Ferroelectrics, and Frequency Control* , vol. 71, no. 1, pp. 153-177, January 2024.

[16] Jian-yu Lu, "A general method to obtain clearer images at a higher resolution than theoretical limit," *186th Meeting of Acoustical Society of America, Acoustical Lay Language Paper* (ALLP), April 22, 2024 (https://acoustics.org/a-general-method-to-obtain-clearer-images-at-a-higher-resolution-than-theoretical-limit/).

[17] Jian-yu Lu, "Remote Super-Resolution Mapping of Wave Fields," *IEEE Transactions on Ultrasonics, Ferroelectrics, and Frequency Control*, vol. 72, no. 3, pp. 370-379, March 2025.

[18] Jian-yu Lu, "Generation of modulators for super-resolution imaging," *Journal of Acoustical Society of America*, vol. 157 no. 4, pt. 2, pp. A56, 2025 (abs) (https://doi.org/10.1121/10.0037370).

[19] Jian-yu Lu, "Focused limited-diffraction beams for ultrasound therapy applications," in *2021 IEEE International Ultrasonics Symposium Proceedings*, pp.1-4, 2021.

[20] Jian-yu Lu, "Producing Bessel beams with an RF transformer," *IEEE Transactions on Ultrasonics, Ferroelectrics, and Frequency Control*, vol. 72, no. 10, pp. 1426-1435, October 2025.

[21] Jian-yu Lu, "Focused beams for high-resolution imaging and other applications." In *Proceedings of Meetings on Acoustics* (POMA), vol. 45, no. 1. AIP Publishing, 2021.

[22] Jian-yu Lu, "Limited diffraction array beams," *International Journal of Imaging System and Technology*, vol. 8, no. 1, pp. 126-136, January 1997 (ISSN: 0899-9457)

[23] M. Xu and L. V. Wang. "Photoacoustic imaging in biomedicine." *Review of scientific instruments* 77, no. 4 (2006).

[24] J. Jodhani, A. Handa, A. Gautam, and R. Rana. "Ultrasonic non-destructive evaluation of composites: A review." *Materials Today: Proceedings* 78 (2023): 627-632.

[25] K. Nightingale. "Acoustic radiation force impulse (ARFI) imaging: a review." *Current medical imaging reviews* 7, no. 4 (2011): 328-339.

[26] S. Peter and R. I. Leine. "Excitation power quantities in phase resonance testing of nonlinear systems with phase-locked-loop excitation." *Mechanical Systems and Signal Processing* 96 (2017): 139-158.

[27] G. T. Mase, R. E. Smelser, and G. E. Mase. *Continuum mechanics for engineers*. CRC press, 2009.

[28] J. W. Goodman. *Introduction to Fourier optics*. Roberts and Company publishers, 2005.

[29] J. D. Achenbach. *Wave propagation in elastic solids*. Elsevier, North-Holland Publishing Company, 1973.

[30] P. M. Morse and H. Feshbach, *Methods of Theoretical Physics*. Part I, McGraw-Hill, New York, 1953.

[31] I. S. Gradshteyn and I. M. Ryzhik, *Table of Integrals, Series, and Products*, 7th Edition, Academic Press, U.K., 2007.

[32] Jian-yu Lu, "An experimental study of focused Bessel beams," in *2025 IEEE International Ultrasonics Symposium Proceedings*, pp. 1-4, 2025 (in press).

[33] J. M. Kweun, H. J. Lee, J. H. Oh, H. M. Seung, and Y. Y. Kim. "Transmodal Fabry-Pérot resonance: theory and realization with elastic metamaterials." *Physical review letters* 118, no. 20 (2017): 205901.

[34] J. Bercoff, M. Tanter, and M. Fink. "Supersonic shear imaging: a new technique for soft tissue elasticity mapping." *IEEE transactions on ultrasonics, ferroelectrics, and frequency control* 51, no. 4 (2004): 396-409.

[35] S. C. Gupta, "Delta function." *IEEE Transactions on Education* 1 (1964): 16-22.